Seasonal influence of the sea surface temperature on the low atmospheric circulation and precipitation in the eastern equatorial Atlantic

Remi Meynadier, Gaëlle de Coëtlogon, Marion Leduc-Leballeur, Laurence Eymard, Serge Janicot

Seasonal influence of the sea surface temperature on the low atmospheric circulation and precipitation in the Eastern Equatorial Atlantic

Rémi Meynadier (1), Gaëlle de Coëtlogon (2), Marion Leduc-Leballeur (3), Laurence Eymard (4) and Serge Janicot (4)

1. LA (Toulouse)
2. LATMOS-IPSL (Paris)
3. LGGE (Grenoble)
4. LOCEAN-IPSL (Paris)

Abstract

The Air-Sea interaction in the Gulf of Guinea and its role in setting precipitation at the Guinean coast is investigated in the present paper. This study is based on satellite observations and WRF simulations forced by different sea surface temperature (SST) patterns. It shows that the seasonal cold tongue setup in the Gulf of Guinea, along with its very active northern front, tends to strongly constrain the low level atmospheric dynamics between the equator and the Guinean coast. Underlying mechanisms including local SST effect on the marine boundary layer stability and hydrostatically-changed meridional pressure gradient through changes in SST gradient are quantified in WRF regarding observations and CFSR reanalyses. Theses mechanisms strongly impact moisture flux convergence near the coast, leading to the installation of the first rainy season of the West African Monsoon (WAM) system. The current study details the mechanisms by which the Atlantic Equatorial cold tongue plays a major role in the pre-onset of the boreal WAM.

1. Introduction

The northern Gulf of Guinea is marked by a heavy coastal rainfall in April – May, which is generally intense during 2 to 3 weeks, and stops about one week before the onset of the Sahelian phase of the West African monsoon (Thorncroft et al. 2010, Nguyen et al. 2011). The latter is suspected to be strongly conditioned by the continent, with an important role played by the Saharan Heat Low in West Africa (Lavaysse et al. 2009). The monsoon jump (i.e the rapid shift of precipitation from the Guinean coast to the Sahel) occurs also because of dynamical instabilities developing at the end of the coastal precipitation phase (Cook 2015). Coastal convection is likely inhibited because of the subsidence of dry air induced by a westward Rossby wave generated after the Indian monsoon onset (Flaounas et al. 2012). It has been shown that the sea surface temperature (SST) in the Gulf of Guinea played a key role in the West African Monsoon. The intensification and the northward seasonal migration of the South Atlantic anticyclone (Sta Helena) induces an acceleration of the Trade winds in the southeastern Tropical Atlantic in boreal spring and summer, cooling the SST into an equatorial "cold tongue" between roughly 4°S and 1°N (Caniaux et al. 2011, Marin et al. 2009, de Coëtlogon et al. 2010, Jouanno et al. 2013, Giordani et al. 2013). A consequence of the northern front of the cold tongue is to accelerate the overlying surface wind, as suggested for interannual (Caniaux et al. 2011) and intraseasonal (de Coëtlogon et al. 2010, 2014) timescales. Moreover, the development of the cold tongue during the boreal spring controls the Guinean coastal rainfall (GCR) in May-June (Thorncroft et al. 2010, Leduc-Leballeur et al. 2011), through the onset of a low-level atmospheric circulation (LLAC) between the equator and the coast (Leduc-Leballeur et al. 2013). The implied mechanism is linked to changes in Sea Level Pressure (SLP) gradient induced by the strengthened meridional SST gradient in the Northern Front of the Cold Tongue (NFCT, de Coëtlogon et al. 2014, Caniaux et al. 2011), according to the mechanism described in Lindzen and Nigam (1987). It then increases the transport of moisture towards the coast (Thorncroft et al., 2010), encouraging convection to develop there. This mechanism will be called afterward "LN" (as "Lindzen and Nigam").

Another mechanism of Tropical Atlantic SST influence on surface wind is linked with the vertical mixing of the wind momentum in the marine atmospheric boundary layer (MABL), which decreases over a colder SST because of an increased stability in the lower atmospheric column (Sweet al. 1981, Wallace et al. 1987, Hayes et al. 1987). Stability is also increased by tropospheric subsidence occurring at the equator, suppressing deep convection when the cold tongue is well established (Yin and Albrecht 2000). This mechanism will be called afterward "SW" (as "Sweet and Wallace"). De Coëtlogon et al. (2014) showed significant hints of both of these mechanisms in daily observations and reanalyses at short timescales (a few days), but not at seasonal timescales. The connection between the NFCT and the GCR is therefore investigated in this study at the seasonal scale.The tested hypothesis is that the NFCT forces both the wind speed increase between the equator and the Guinean coast, and the northward migration of the precipitation toward the coastal region. Numerical simulations are performed with the non-hydrostatic regional Weather Research and Forecasting WRF model (Skamarock et al., 2008) forced by different observed SST. The analysis aims at quantifying the cold tongue influence on low level dynamics and further explore its impact on the water cycle.

The numerical simulations discussed in this paper are based on composites around a reference date, thereafter Tref, of the LLAC and Guinean coastal rainfall (GCR) onset, which was defined in Leduc-Leballeur et al. (2013). Section 3 thoroughly describes the Tref definition and the air-sea coupling for a 2-month composite period around Tref in the observations, the meteorological reanalyses, and the WRF simulations. Section 4 focuses on the mechanisms modifying the low-level atmospheric circulation induced by SST seasonal variability and the quantitative estimation of the underlying processes in the WRF simulation. The importance of the atmospheric forcing at the model domain boundaries versus the SST influence are tested in four additional experiments, detailed in section 5. The last section presents a short discussion and summary of the results.

2. Data

Surface wind vectors were provided by the QuikSCAT (Quick Scatterometer) satellite (Liu et al. 2000) available on the Remote Sensing Systems website (www.remss.com), as 3-day running mean on a 0.25°x0.25° grid between 2000 and 2009. A two-dimensional cubic-spline interpolation first filled the gaps due to the clouds for each available day, and then a linear temporal interpolation at each grid point completed the 15 missing days over the decade.

The high-resolution SST product developed using optimum interpolation, the Advanced Very High Resolution Radiometer (AVHRR) infrared satellite SST data, and in situ data from ships and buoys (Reynolds et al. 2007) have been retrieved thanks to the NOAA-NCDC (National Oceanic and Atmospheric Administration - National Climatic Data Center) ftp site (http://www.ncdc.noaa.gov), with a spatial grid resolution of 0.25° and at a daily temporal resolution.

In addition, the daily averaged TRMM 3B42 V7 product on a 0.25° x 0.25° grid was used. It mixes satellite measurements from microwave sensors and infrared geostationary instruments with data from ground radars (Huffman et al. 2007), which guarantees the best possible quality for precipitation data. It was retrieved from the website trmm.gsfc.nasa.gov.

Reanalysis from the Climate Forecast System Reanalysis (CFSR, Saha et al. 2010) were retrieved from the National Centre for Environmental Prediction (NCEP) site (*www.ncep.noaa.gov*). One of the distinctive CFSR characteristics is that it was performed with a coupled ocean-atmosphere model, which was shown to better describe the air-sea interaction in the eastern Tropical Atlantic than the ERA-interim (European centre for meddium-range weather forecasts Re-Analysis, de Coëtlogon et al. 2014). The data are available on a 0.5°x0.5° horizontal grid, with vertical atmospheric profiles retrieved on 27 levels from 1000 to 100 hPa. Daily means of the 6-hourly parameters were used over the

106 2000-2009 decade.

107

108 **3. Composites around the LLAC / GCR onset date (Tref)**

109 *a. Observations composite*

110 Leduc-Leballeur et al. (2013) defined a reference date to study the abrupt change observed in
111 the surface wind pattern between April and July in the eastern equatorial Atlantic, due to the
112 cold tongue and NFCT development. This date, hereafter referred as Tref, corresponds to the
113 onset of strong southerlies between the equator and the Guinean coast (more exactly, Tref is
114 the date when southerlies become - and remain until fall - stronger at 2°N-3°N than just south
115 of the equator, see their paper for more details). They showed that this date corresponds to the
116 GCR onset using satellite precipitation data, and to the LLAC installation between the equator
117 and the Guinean coast as seen in atmospheric reanalyses (NCEP CFSR and ERA-Interim).
118 Fig. 1 defines the Tref date for each year, from 2000 to 2009. Among them, note two
119 particular years : the earliest Tref in 2005 (May 11), and the latest in 2006 (June 25). Note that
120 years 2005 and 2006 are known for exhibiting a large difference in the properties of the
121 equatorial cold tongue. Marin et al. (2009) showed that far colder temperatures were observed
122 in 2005 than in 2006. This difference results mainly from a time shift in the development of
123 the cold tongue between the two years, due to different surface wind speed conditions in
124 April-May, thus explaining why Tref is earlier in 2005 than in 2006. This large interannual
125 variability prevents the regular daily seasonal average in May-June of being pertinent for a
126 clear view of the seasonal changes in the observations, hence the need for a composite built
127 around Tref.

128 The seasonal composite around Tref (i.e. daily averages around Tref for the period 2000-
129 2009) marks clearly the time of a strong SST cooling between roughly 4°S and 1°N (Fig. 3
130 bottom row), while the wind accelerates north of the equator and decelerates further south
131 (middle row). In addition, Tref corresponds to a northward seasonal shift of the rainfall (top
132 row): after Tref, no more rainfall is indeed observed south of 2°N in the Gulf of Guinea. The

intense GCR lasts about 2 weeks before the Sahelian “monsoon jump”. In this composite, the mean observed seasonal GCR clearly lasts about 2 weeks, while the rain completely stops south of 2°N-3°N (top left). The coastal shift of precipitation also coincides with the intensification of the oceanic NFCT (more than 0.6 K per lat. deg. after Tref, bottom left).

In addition to this clear seasonal evolution around Tref, a very large intraseasonal variability can be observed yearly (not shown) in the equatorial region and further south, with a dominant timescale of about 2 weeks, which is probably due to a strong SST / surface wind coupling (with a negative feedback) in the equatorial region (see de Coëtlogon et al. 2010, 2014). Although these quasi-biweekly timescales are considerably damped in the 2000-2009 composites around Tref, as seen in Fig. 3 (left column), they are however still visible in the observed surface wind and SST composites, emphasizing the importance of the quasi-biweekly oscillations for the phasing of the GCR onset, as discussed in Leduc-Leballeur et al. (2013). However, the intraseasonal variability will not be further discussed here, as the scope of this study is to rule out the mechanisms behind the rapid seasonal shift around Tref.

b. WRF simulation and CFSR composites

The configuration of WRF version 3.3 and parameterizations used in this study are chosen to produce realistic surface wind and rainfall patterns in May – June (see Meynadier et al. 2014). WRF physics is based here on Betts-Miller-Janjic (Betts,1986 ; Betts et Miller, 1986 ; Janjic , 1994) scheme for the cumulus scheme, Yonsei University (YSU, Hong et al., 2006a) non-local closure PBL scheme, RRTMG for the short and long-wave radiation schemes and the single moment six-class (WSM6) scheme (Hong et al., 2006b) for microphysics. The horizontal resolution is set at 25 km with 35 vertical sigma levels and a top-of-atmosphere at 50 hPa. The simulation domain is similar to the one used in Meynadier et al. (2014) and was chosen to be wide enough in latitude and longitude for WRF to fully simulate "by itself" the large scale atmospheric features (such as the African Easterly Jet) of the West African climate system.

A 2-month numerical simulation with WRF was designed to represent the average seasonal

160 evolution around Tref. ERA Interim data for years 2000 to 2009 were averaged in 6-hour
161 composites around Tref (1 month before and 1 month after), and used to force the regional
162 model boundaries, except for the SST field. For the latter, the surface input forcing over the
163 ocean was composited around Tref using satellite-based daily Reynolds dataset (seen in Fig.
164 3, bottom row).

165 A time-latitude diagram of this WRF simulation for the 10°W-0 meridional band shows that
166 the precipitation simulated by the model is almost twice too abundant. Its evolution during the
167 seasonal transition (phasing around Tref + latitudinal distribution) matches the observed
168 composite quite well (Fig. 3, top middle). The evolution of the simulated surface wind pattern
169 is also in agreement with the observations, except that the wind speed is about 1 to 3 m/s too
170 weak (middle row). This northerly bias is the strongest between the equator and the Guinean
171 coast, where the actual southerlies can actually reach 8 m/s on average. A similar bias was
172 also found in reanalyses (see de Coëtlogon et al. 2014), as can be seen here for the CFSR
173 reanalyses (Fig. 3, right column), in spite of the assimilation of QuikSCAT surface wind
174 observations. One can note that WRF SST is not exactly similar to Reynolds SST used to
175 force the model but shows slightly smaller values. WRF SST shown here is actually surface
176 skin temperature (SKT) from the WRF ouput.

177 *c. Transition patterns around the LLAC onset*

178 The abrupt seasonal transition around Tref was examined by comparing the parameters at two
179 different times, before and after Tref:

180 period 1 = [Tref–3 weeks : Tref–1 week]. On average : 10-24 May.

181 period 2 = [Tref : Tref+2 weeks]. On average : 1-14 June.

182 The two periods (also sketched in Fig. 1) are 2 weeks long each, thereby partly damping the
183 large quasi-biweekly variability observed in the equatorial region.

184 Fig. 4 (surface wind and SST) and Fig. 5 (precipitation and precipitable water, thereafter

PWAT) show the parameters averaged within each of these two periods, as well as their difference (i.e. [period 2] minus [period 1]). The top row shows the observations, the middle row shows the WRF simulation, and the bottom row shows the wind bias in the model relative to the observations.

The surface wind speed is generally too weak in the simulation, as mentioned in the previous section, by about 1 m/s, and up to 3 m/s north of the equator (Fig. 4, bottom row). Before Tref (period 1), this bias stands south of 5°N, with a slightly stronger-than-normal wind near the Guinean coast; but after Tref, the bias largely increases near the coast (period 2). Since the wind bias is actually maximal downstream of the SST front, particularly after Tref near the coast, it may suggest that the NFCT impact on the surface wind acceleration is not strong enough in the model,compared to the observations. The bias could also come from flaws in the forcing fields at the model boundaries, or from the model itself, especially near West Africa coast, where the numerical representation of the continental surface wet conditions still remains a challenge (Taylor 2008) and could impact the near-shore low-level atmospheric circulation.

Although much too abundant in the simulation, the precipitation spatial distribution is very similar to the observations (Fig. 5): with a realistic slight deviation from the zonal symmetry, it exhibits a clear northward migration from as far south as the equator before Tref to a maximum near the Guinean coast after Tref, and no more rainfall south of 2-3°N. The PWAT pattern also follows this steep northward shift before and after Tref, with a pattern similar in the simulation than in the observations, pending a small dry bias.

Let us remind here the two main mechanisms through which the SST possibly influences the surface wind:

* Sweet and Wallace (**SW)** mechanism: the cold tongue reduces the wind speed through the vertical stability of the lower atmospheric boundary layer. As discussed for example in de Coëtlogon et al. (2014), this effect is immediate and local, and confined in the lower part of

211 the boundary layer (or mixed layer), and it is well observed in the vicinity of the cold tongue,
212 where the SST cooling and wind speed weakening are maximal (i.e. in the [1°S-Eq] band).

213 * Lindzen and Nigam (**LN)** mechanism: an increased SST gradient accelerates the overlying
214 wind through a hydrostatically-induced increased pressure gradient (in absolute values),
215 possibly advected by the mean atmospheric flow. Here, on average, the meridional SST
216 gradient is maximal in [Eq-1°N], and the southerlies crossing the equator in [2.5°N-3.5°N]
217 (i.e. 100 to 200 km downstream of the SST front).

218 The vertical extension of the SST impact is documented with latitudinal-vertical sections of
219 the model output, averaged between 10°W and 0°E. Fig. 6 shows period 1, period 2, and their
220 difference (i.e. [period 2] minus [period 1]), for the meridional velocity (shadings) and
221 meridional gradient of geopotential height (thereafter dZ/dy, black contours) up to 500 hPa. It
222 shows that dZ/dy is negative south of the equator in the whole troposphere, traducing the
223 presence of the South Atlantic anticyclone (Fig. 6a and 6b). But further north, close to and
224 over the continent (north of 5°N), its pattern is more complex than would give a "classical
225 Hadley circulation", with a symetric positive dZ/dy: because of the strong meridional thermal
226 contrast between the eastern Tropical Atlantic and West Africa, dZ/dy is strongly negative
227 within or near the atmospheric boundary layer, and strongly positive overhead.

228 The seasonal abrupt transition of the meridional low-level atmospheric circulation from
229 period 1 to period 2 is clearly seen in Fig. 6: the middle of the LLAC (i.e. subsident/
230 convective cell between the equator and the Guinean coast) is indeed shifted from around
231 0.5°N in period 1 to around 2°N in period 2 (Fig. 6a and 6b), thereby strongly increasing the
232 subsidence, or inhibiting the convection, between the equator and 3°N, and increasing the
233 convection north of 4°N (Fig. 6c). The difference in time (period 2 minus period 1, or Δ)
234 of the meridional SST gradient (dSST/dy) in Fig. 6d fits very well the pattern of Δ dZ/dy:
235 the largest value of |dZ/dy| is indeed found between 1°N and 2°N, slightly north of the Δ
236 dSST/dy maximum at 0.5°N-1°N: this is in agreement with a pressure anomaly forced by the

SST front through the LN mechanism, which likely controls the strong northward acceleration of southerlies between the equator and the coast. The impact of the SST front extends up to 850 hPa at 1°N, which is even deeper than the boundary layer (which top is usually around 900 – 950 hPa, not shown). Conversely, south of the front (4°S-Eq), the pressure gradient slightly loosens, with a pattern matching the decrease in dSST/dy, which weakens down the southerlies, but within a much shallower layer. The latter signal is in agreement with the LN mechanism, but it also fits with the SW mechanism between 2°S and the equator, just over the coldest part of the cold tongue, where only a thin surface layer (under 975 hPa) seems influenced. As was previously found in the observations (de Coëtlogon et al. 2014), both mechanisms appear indeed to control the surface wind in this area, with a time lag spanning from a few hours (when the SW dominates) to 1 - 2 days (when the LN takes control).In summary, the surface divergence induced by the SST front (seemingly through both SW and LN mechanisms) around the equator creates a strong anomalous secondary circulation in the low troposphere (< 700 hPa), subsiding at the equator and convecting at the coast, as well as a strong deep subsidence over the NFCT. This is in very good agreement with the LLAC found in ERA-interim and CFSR reanalyses, as described in Leduc-Leballeur et al. (2013): before Tref, they found a large loop subsiding over the Gulf of Guinea south of 2°S and convecting between the equator and the coast, with a northward monsoon flux near the surface and a return southward branch around 700 mb. But after Tref, the LLAC is framed between the equator and the coast, with its southern edge probably pushed north by the NFCT.

This seasonal shift of the LLAC in the Gulf of Guinea has a strong effect on precipitation, as Fig. 5 already suggested. In addition, Fig. 7 presents the vertical cross-section of meridional-vertical wind vectors and horizontal moisture flux divergence, highlighting the large control of the latter on the precipitation profiles, averaged between 10°W and 0°E. Before Tref, a low-level divergent / convergent humidity flux pattern straddles the equator in the low atmosphere (<850 hPa). As suggested in Thorncroft et al. (2010), the SST between the equator and 3°N is warmer than 28°C (see Fig. 3), which can trigger deep atmospheric convection: the convergence maximum is located just south of 3°N, framed by two divergent

areas (south of the equator and north of 4°N), in agreement with the diabatic heating described for example in Gill (1981). After Tref, the SST cooling within the cold tongue leads the southerlies strengthening north of the SST front (or NFCT) as discussed previously, hence to the reinforcement of the divergent pattern and its northward shift by more than 200 km, at the equator. This likely leads the atmospheric subsident branch to migrate northward, up to 2°N, thereby reinforcing the moist convection inhibition (in addition to the SST cooling).

A strong reinforcement of the low-level moisture flux convergence is also visible between 3°N and 5°N: it results from the wind strenghtening around 3°N on the one hand, and the deceleration of the low-level wind as the air moves toward the Guinean coast at 4°N-5°N on the other hand.

The latter probably comes from an increased coastal convergence, since the continental surface friction considerably weakens the surface wind (and if the upstream wind is stronger, then the deceleration due to the continental friction is larger as well, thereby increasing the convergence). But in addition, there is also a clear positive dZ/dy signal that counters southerlies north of about 3.5°N (Fig. 6c), with maximal values on the continental side of the Guinean coast, of comparable magnitude than the ones created by the NFCT: clearly, this dZ/dy inversion around 3.5°N is a major contributor of the low-level convergence between 3°N and 5°N after Tref.

Very interestingly, the continental dZ/dy maximal values, around 5.5°N and 6.5°N, coincide with huge negative peaks in the meridional gradient of SKT (Fig. 6, bottom). This suggests that a flaw in the representation of the WRF wet continental conditions (or from the too-abundant precipitation ?) may well explain the strong northerly bias in the model surface wind north of 5°N after Tref, in comparison with satellite data, with a too-strong dZ/dy inversion close to the Guinean coast.

Note that the patterns of the atmospheric mass divergence and of the humidity flux divergence are very similar (not shown), which emphasizes the fact that the precipitation are strongly controlled by the low-level atmospheric dynamics in this region. If thermodynamics are likely

important before Tref for driving the deep atmospheric convection (precipitation oceanic phase described in Thorncroft et al. 2010 and Nguyen et al. 2011), these results strongly suggests that the NFCT apparition drives the increased coastal convergence and the Guinean coastal rainfall after Tref.

4. Quantitative estimations of the SST influence on surface wind

In order to compare the simulation with observations more easily, we attempt here to quantify the impact of the SST and dSST/dy on the surface wind speed where their influence is maximal: the cold tongue for SST, and its northern front for dSST/dy.

Surface wind speed, SST and dSST/dy were zonally averaged between 10°W and 0°E, in three different latitude bands: 1°S-Eq (SST + wind speed), Eq-1°N (dSST/dy), and 2.5°N-3.5°N (wind speed). This leads to 61 daily values around Tref (i.e. from Tref – 30 days until Tref + 30 days), from the 2-months WRF simulation, or from the composites computed with observations and CFSR reanalysis.

A linear regression was performed on the surface wind speed versus SST in the [1°S-Eq] band, allowing to estimate the amplitude of the local wind response to the small-scale SST features within a few hours through the SW mechanism (Fig. 8, left). Note that before Tref, the equatorial SST is rather uniformly warm: the equatorial wind is then mostly driven by the large-scale atmospheric circulation. Only post-Tref values were therefore taken into account for the linear regression fits (i.e. days plotted with dots in Fig. 8, left, whereas circles represent the days before Tref). In the observations, the SST / wind speed fit has a slope of almost 1 m/s/K, which indicates a cooling of the SST by about 1K inducing a weaker wind speed by more than 1 m/s (blue line). De Coëtlogon et al. (2014) found that both ERA-Interim and CFSR tend to underestimate the wind response to the SST fluctuations at intraseasonal timescales, which is also found here at the seasonal scale with a slope of less than ½ m/s/K for CFSR (green line). On the contrary, the WRF model exhibits a decreased wind when the

12

318 SST has cooled down with a slope slightly larger than 1 m/s/K, which broadly fits the
319 observations pending uncertainties (red line).

320 The surface wind response to dSST/dy through the LN mechanism was similarly estimated,
321 but in taking into account the delayed response in time (1-2 days) and space (advection by the
322 mean atmospheric flow, Fig. 8, right): dSST/dy is then averaged in [Eq-1°N], and the wind
323 response is measured by substracting the wind speed just south of the front (at [1°S-Eq]) from
324 the wind speed further north (at [2.5°N-3.5°]), thereby isolating the wind strenghtening due to
325 the SST gradient from the large-scale atmospheric circulation.

326 The regression fit matches very well the observations, with a slope of 4 to 5 m.(lat. deg.)/s/K
327 (Fig. 8 right, simulation in red and observations in blue), whereas the CFSR reanalysis clearly
328 appears to underestimate the mechanism amplitude (green line). This suggests that the wind
329 strenghtening when crossing the NFCT (due to the LN mechanism) in the model is in good
330 agreement with the observations. Note that the set of WRF parameterizations were carefully
331 chosen in order to get the characteristic weak / strong seasonal wind pattern on each side of
332 the NFCT (Meynadier et al. 2014), but this did not guarantee to get realistic linear amplitudes
333 of the wind response to both LN and SW forcing mechanisms.

334 The surface wind is usually considered as resulting from a balance between the pressure
335 gradient force, the Coriolis force, and the friction forces (drag at the surface, and momentum
336 entrainment from the wind shear above), usually neglecting the advection (inertial) term, as in
337 the simple model of Stevens et al. (2002). The SST influences the wind through a local
338 modification of the pressure gradient (LN mechanism), opposing the large-scale pressure
339 gradient - rather controlled by the free troposphere above the MABL. In addition, through the
340 SW mechanism and the stratification in the MABL, the SST partly controls the momentum
341 entrainment from above. Therefore, a flaw in the representation of the atmospheric circulation
342 in the free troposphere, above the MABL top – where the vertical gradients, such as humidity
343 gradient are very strong (Meynadier et al 2014), - could have a large impact on the surface
344 wind representation. Eventually, we found that the horizontal advection (inertial) term

345 $\vec{U}.\nabla\vec{U}$ is also very important for this region in the WRF simulation. Fig. 9 shows its
346 mean value during the 2-month simulation: it can amount to as much as half of the pressure

347 gradient magnitude $\frac{1}{\rho}\|\nabla SLP\|$, as shown in Fig. 9. In particular, this ratio is of about
348 35% around 3°N between 10°W and 0°E on average in the 2-month simulation, with a larger
349 value (up to 50%) if period 2 only is considered, because the wind is stronger (not shown).
350 The advection is therefore actually far from being negligible in the Eastern Equatorial
351 Atlantic, compared to SST or free troposphere influences, which would probably reinforce
352 any bias induced by the representation of these 2 terms.

353 In short, the SST influence on the surface wind appears to match well the observations in
354 agreement with the SW and LN mechanisms amplitudes. But quite strong biases remain in the
355 surface wind model compared to the observations, which questions the influence of larger-
356 scale environmental factors, such as the free tropospheric circulation or the continental
357 surface. In particular, the next section investigates if the characteristic wind pattern evolution
358 around Tref is actually due to the cold tongue development in the SST, or rather to a remote
359 forcing.

360

361 **5. Sensitivity cross-experiments : SST vs external forcing**

362 In order to test if the results of previous sections are really due to the change in SST, and not
363 to the change in the forcing parameters at the model boundaries, four additional WRF
364 simulations were performed. All were made with a stationary external forcing, averaged either
365 in period 1 (before Tref) or in period 2 (after Tref), with a permanent diurnal cycle (the same
366 composite day of period 1 was repeated during 8 weeks, and the same was done for the
367 composite day of period 2):

368 * external forcing of period 1 with the SST of period 1 (thereafter “case1”)

369 * external forcing of period 2 with the SST of period 2 (thereafter “case2”),

* external forcing of period 1 with the SST of period 2 (thereafter “case1_SST2”),

* external forcing of period 2 with the SST of period 1 (thereafter “case2_SST1”).

This way, the influence of the SST change can be tested in the conditions of constant period 1 or constant period 2, i.e. without any change in the external forcing (case1_SST2 minus case1, or case2 minus case2_SST1), whereas the influence of the external forcing can be tested in the conditions of a constant SST (case2_SST1 minus case1, or case2 minus case1_SST2). Indeed these effects are certainly not completely linear, and the method misses their non-linear dynamics, but some of their main characteristics can nonetheless be depicted.

The significance of these differences were validated by a t-test, based on rms estimated for case1 and case2 simulations, the maximal value between the 2 being kept at each grid point. One degree of freedom per day was taken (which correspond to an exponential decrease of less than one day in autocorrelations, checked for a few SLP and meridional surface wind gridpoints, not shown). The null hypothesis (i.e. non significant difference between the 2 values) was only rejected when the difference exceeded the 95% t-value, thereby taking into account the large level of noise in the simulations due to internal variability in the model.

Fig. 10 shows the difference in SLP patterns due to a change in SST (top row) or in the external forcing (bottom row). The seasonal evolution of the SLP is clearly due to the SST change, since the maximal SLP fluctuations (1 to 1.5 mb) are located close to the minimal SST ones for both periods (about -2K, as shown in black contours). In the simulations only differing by the external forcing (the SST is the same), the SLP does not increase significantly in the equatorial region (bottom row), by less than 0.3 – 0.4 mb. Only the southern Eastern Equatorial Atlantic (south of 5°S) appears significantly influenced by the external forcing.

The impact of the SST vs the external forcing is also shown in Fig. 11: there again, the northward wind acceleration between the equator and the coast appears very clearly due to the SST change. Shadings indicate the change in the meridional SLP gradient (thereafter

396 dSLP/dy): the northward wind acceleration can clearly be attributed to a larger than normal
397 SLP gradient (in magnitude) toward the continent, with a maximum in the NFCT area -
398 around 0.5°N-1°N (Fig. 11, top row), thereby illustrating the LN mechanism previously
399 described. Note that the |dSLP/dy| maximum is located slightly north of the NFCT, and the
400 wind acceleration maximum even further north (between 3°N and 4°N), likely because of an
401 important advection by the mean flow as discussed previously.

402 South of the NFCT, and as expected from this side of the front (where dSST/dY <0), the
403 weaker |dSLP/dY| (by about 0.05 mb per lat. deg.) induces a generally weaker wind south of
404 the equator, by up to 1 m/s (Fig. 11, top row). Moreover, the general strengthening of the
405 external boundary wind forcing, from period 1 to period 2, generates opposite (stronger) wind
406 anomalies of smaller magnitude (Fig. 11, bottom row). Note that these two different forcings
407 result into a rather modest weakening of the wind south of the equator, from period 1 to
408 period 2, in the WRF composite simulation discussed in previous sections (as seen for
409 example in Fig. 4, middle right), which would interestingly suggest that the seasonal
410 reinforcement of the Trade winds in the southeastern Tropical Atlantic by the northward
411 migration of the InterTropical Convergence Zone can be largely damped as far south as 7°S
412 by the cold tongue development.

413 Cross-test experiments were also investigated vertically: they show that the NFCT impact is
414 very strong around the equator, and significant from as far south as 6°S, up to the coast at 5°N
415 (not shown). However, the strong signals seen over the continent in Fig. 6 and 7 (north of
416 5°N) appear due to the seasonal change of the external forcing (surface conditions ?), and
417 probably to the Saharan Heat Low reinforcement as well in period 2 (not shown).

418 Cross-test experiments were then analyzed regarding the water cycle components. Figure 12b
419 clearly shows that with the set-up of the NFCT, the SST seasonal evolution solely pushes
420 precipitation toward the Guinean coast and suppresses moist convection south of 4°N.
421 Precipitation patterns are spatially well correlated with vertically integrated moisture flux
422 anomalies (figure 12 a and b). In term of spatial structures and amplitude, the change of

423 moisture flux convergence (or divergence) due to the change of SST exhibits indeed a very
424 consistent pattern with the rainfall changes. Note that the vertically integrated moisture flux
425 field (represented by vectors in Figure 12a) is very close to the surface wind pattern due to
426 dSLP/dy: change before and after Tref in moisture flux convergence or divergence (and then
427 precipitation) is directly connected to the low-level wind changes due to the SST seasonal
428 evolution. The vertical structure of moisture convergence (Figure 12c) confirms the influence
429 of the SST changes over the ocean, even if the amplitude of the low level moisture divergence
430 and the associated suppressed rain (between the equator and 3°N) is likely overestimated,
431 compared to Fig. 7 (right panel). An explanation of this could be that the simulation with
432 everyday similar warm SST forcing before Tref leads to large amount of ocean precipitation
433 using the BMJ cumulus scheme.

434

435 **6. Conclusion**

436 The air-sea interaction mechanisms in the Gulf of Guinea and their role in the coastal
437 precipitation are investigated from WRF experimental simulations. It is shown here that the
438 WRF simulation captures very well the seasonal transition of the rainfall from an oceanic
439 phase to the Guinean coastal one, as well as the transition of the surface wind speed from a
440 rather uniform distribution in the gulf of Guinea to a very characteristic pattern across the
441 NFCT (weak around the equator, strong further north). The increased low-level convergence
442 near the coast has for effect to set the Guinean coastal rainfall described in Nguyen et al.
443 (2011). Boundary and lateral forcing cross-test experiments made with WRF clearly show
444 that the SST seasonal evolution solely pushes precipitation toward the Guinean coast and
445 suppresses moist convection south of 4°N. This is due to a change in moisture flux
446 convergence directly connected to the low-level wind changes under the influence of the SST
447 seasonal variability.

448 The amplitude of the seasonal cold tongue impact on surface wind through the SW
449 mechanism is estimated with linear regression, leading to a value of about 1 m/s/K, in

agreement with the estimations made at intraseasonal timescales in de Coëtlogon et al. (2014). It is about twice as large as the SST impact on the overlying wind speed as measured in extratropical regions (Perlin et al. 2014, Small 2008). In addition, through the LN mechanism, the NFCT accelerates the surface wind by 4 to 5 m.(lat. deg.)/s/K. These values compare very well with the ones found in the observations, whereas the CFSR reanalysis exhibits a clear tendency to underestimate the impact of both mechanisms, which is consistent with the northerly surface wind bias found between the equator and the coast in the reanalysis and may be partly due to a lower resolution (de Coëtlogon et al., 2014). However, putting aside the hypothesis that observations could be wrong there (since the QuikSCAT product is known to be taken with great cautions in the 100-km band off the coasts, as all scatterometers products), a similar strong northerly wind bias is also found in the WRF simulation in the northern Gulf of Guinea. As discussed in section 3c, the latter is likely linked to a strong decrease in the meridional gradient of the low-level pressure near the Guinean coast in the WRF simulation after Tref (Fig. 6c), which would excessively weaken down the upstream marine southerlies north of 3.5°N. This large change in the meridional pressure gradient seems to be of inland origin, which could suggest a flaw in the model representation of the continental response to excessive coastal convergence and convection in the Guinean coastal region in the model. This flaw could also explain why the secondary circulation between the equator and the coast, or LLAC, after Tref, appears to be weaker in the model than in the reanalyses (ERA interim as well as CFSR), since this cell variability is probably driven not only by the surface pressure gradients but also by internal thermodynamics (it would indeed be partly driven by the humidity convergence at the coast, see Leduc-Leballeur et al. 2013 or de Coëtlogon et al. 2014). Eventually, it is important to keep in mind that the advection of momentum by the mean atmospheric flow plays a very significant role in the cold tongue region.

Unhappily, too few observations of the low troposphere are available in this region to properly document the LLAC, whith only a few radiosoundings launched from the AMMA 2006 (EGEE) and PIRATA 2014 campaigns. Further investigations and a better documentation of the low troposphere dynamics in the northern Gulf of Guinea are therefore

18

strongly needed regarding the structure of the LLAC, especially after Tref, since its misrepresentation could be a clue in the general difficulty of the models to correctly represent the West African Monsoon later on in the season (by, for example, advecting not enough moisture from the Gulf).

19

483 References

484 Caniaux G, Giordani H, Redelsperger J-L, Guichard F, Key E, Wade M. 2011. Coupling
485 between the Atlantic cold tongue and the West African monsoon in boreal spring and summer.
486 *J. Geophys. Res.* **116**: C04003, DOI: 10.1029/2010JC006570.Cook, K.H., 2015 : Role of
487 inertial instability in the West African monsoon jump. *J. Geophys. Res.,*
488 10.1002/2014JD022579

489 De Coëtlogon, G., S. Janico et A. Lazar, 2010 : Intraseasonal variability of the ocean-
490 atmosphere coupling in the Gulf of Guinea during boreal spring and summer. Quart. J. Roy.
491 Meteor. Soc., 136, S1, 426-441.

492 De Coëtlogon, G., and co-authors, 2014: Atmospheric response to sea surface temperature in
493 the Eastern Equatorial Atlantic at quasi-biweekly timescales. Quart. J. Roy. Meteor. Soc.,
494 140: 1700–1714. doi: 10.1002/qj.2250.

495 Flaounas, E., S. Janicot, S. Bastin, and R. Roca (2012), The West African monsoon onset in
496 2006: Sensitivity to surface albedo, orography, SST and synoptic dry-air intrusions using
497 WRF, *Clim. Dyn.,* 38, 685–708.

498 Giordani, H., G. Caniaux, and A. Voldoire, 2013 : Intraseasonal mixed layer heat budget in
499 the equatorial Atlantic during the cold tongue development in 2006. *J. Geophys. Res.,*
500 doi :10.1029/2012JC008280, 118, 650-671.

501 Hayes SP, McPhaden MJ, Wallace JM. 1989. The in uence of sea-surface temperature on
502 surface wind in the eastern equatorial Paci c: Weekly to monthly variability. J. Climate 2:
503 1500–1506.

504 Huffman GJ, Adler RF, Bolvin DT, Gu G, Nelkin EJ, Bowman KP, Hong Y, Stocker EF and
505 Wolff DB., 2007: The TRMM Multisatellite Precipitation Analysis (TMPA): Quasi-global,
506 multiyear, combined-sensor precipitation estimates at ne scales. J. Hydrometeorol. 8: 38–55.

507 Jouanno J., F. Marin, Y. du Penhoat, and J.M Molines, 2013: Intraseasonal Modulation of the
508 Surface Cooling in the Gulf of Guinea. *J. Phys. Oceanogr.*, **43**, 382–401.

509 Lavaysse C, Flamant C, Janicot S, Parker D, Lafore JP, Sultan B, Pelon J (2009) Seasonal
510 cycle of the West African heat low: a climatological perspective. Clim Dyn.
511 doi:10.1007/s00382- 009-0553-4

512 Leduc-Leballeur, M., L. Eymard et G. De Coëtlogon, 2011 : Observation of the marine
513 atmospheric boundary layer in the Gulf of Guinea during the 2006 boreal spring. *Quart. J.*
514 *Roy. Meteor. Soc.*, 137, 657, 992-1003.

515 Leduc-Leballeur, M., G. De Coëtlogon, et L. Eymard, 2013 : Air-sea interaction in the gulf of
516 Guinea at intraseasonal time-scales : wind bursts and coastal precipitation in boreal spring.
517 *Quart. J. Roy. Meteor. Soc.,* 139, 671, 387-400.

518 Lindzen R. S. and Nigam S. 1987. On the role of sea surface temperature gradients in forcing
519 low-level winds and convergence in the tropics. *J. Atmos. Sci.*, 44(17) : 2418–2436.

520 Liu WT, Xie X, Polito PS, Xie S-P, Hashizume H. 2000. Atmospheric manifestation of
521 tropical instability wave observed by QuikSCAT and Tropical Rain Measuring Mission.
522 Geophys. Res. Lett. 27: 2545–2548.

523 Marin F., Caniaux G., Bourles B.,Giordani H., GouriouY., Key E. 2009.Why were sea surface
524 temperatures so different in the eastern equatorial Atlantic in June 2005 and 2006? *J. Phys.*
525 *Oceanogr.* **39**: 1416–1431.

526 Meynadier R., G. de Coetlogon, S. Bastin, L. Eymard, S. Janicot, 2014. Sensitivity testing of
527 WRF parametrizations on air-sea interaction and its impact on water cycle in the gulf of
528 Guinea, Quarterly Journal of the Royal Meteorological Society, DOI :10.1002/qj.2483.

529 Nguyen, H., C. D. Thorncroft, and C. Zhang (2011), Guinean coast rainfall of the West
530 African monsoon, Q. J. R. Meteorol. Soc., 137, 1828–1840.

531 Perlin, N., S ; P. de Szoeke, D ; B. Chelton, R. M. Samelson, E. D. Skyllingstad and L. W.
532 O'Neill, 2014: Modeling the Atmospheric Boundary Layer Wind Response to Mesoscale Sea
533 Surface Temperature Perturbations. *Mon. Wea. Rev.*, **142**, 4284–4307. doi:
534 http://dx.doi.org/10.1175/MWR-D-13-00332.1.

535 Reynolds RW, Smith TM, Liu C, Chelton DB, Caset KS, Schlax MG. 2007. Daily high-
536 resolution blended analyses for sea surface temperature. J. Clim. 20: 5473–5496.

537 Saha S, Moorthi S, Pan H, Wu X, Wang J, Nadiga S, Tripp P, Kistler R, Woollen J, Behringer
538 D, Liu H, Stokes D, Grumbine R, Gayno G, Wang J, Hou Y, Chuang H, Juang H, Sela J,
539 Iredell M, Treadon R, Kleist D, Van Delst P, Keyser D, Derber J, Ek M, Meng J, Wei H, Yang
540 R, Lord S, van den Dool H, Kumar A, Wang W, Long C, Chelliah M, Xue Y, Huang B,
541 Schemm J, Ebisuzaki W, Lin R, Xie P, Chen M, Zhou S, Higgins W, Zou C, Liu Q, Chen Y,
542 Han Y, Cucurull L, Reynolds R, Rutledge G, Goldberg M. 2010b. Supplement to The NCEP
543 Climate Forecast System Reanalysis. Bull. Am. Meteorol. Soc., 91,1015-1057.

544 Skamarock WC, Klemp JB, Dudhia J, Gill DO, Barker DM, Duda MG, Huang XY, Wang W,
545 Powers JG. 2008. 'A description of the advanced research WRF version 3'. NCAR Technical
546 Note-475+STR. NCAR: Boulder, CO. http://www.mmm.ucar.edu/wrf/users/docs/arw v3.pdf
547 (accessed 20 October 2014).

548 Small R.J., de Szoeke SP, Xie SP, O'Neill L, Seo H, Song Q, Cornillon P, Spall M, Minobe S.
549 2008. Air sea interaction over ocean fronts and eddies. *Dynam. Atmos. Oceans* **45**: 274–319.

550 Sweet W., Fett R., Kerling J. et La Violette P. 1981. Air-Sea Interaction Effects in the Lower
551 Troposphere Across the North Wall of the Gulf Stream. *Mon. Wea. Rev.*, 109(5) : 1042–1052.

552 Thorncroft, C. D., H. Nguyen, C. Zhang, and P. Payrille (2011), Annual cycle of the West
553 African monsoon: Regional circulations and associated water vapour transport, Q. J. R.
554 Meteorol. Soc., 137, 129–147.

555 Wallace J. M., Mitchell T. P. et Deser C. 1989. The influence of sea-surface temperature on
556 surface wind in the eastern equatorial Pacific : seasonal and interannual variability. *J. Clim.*,
557 2(12) : 1492–1499.

558 Yin, B. and B. A. Albrecht, 2000: Spatial Variability of Atmospheric Boundary Layer
559 Structure over the Eastern Equatorial Pacific. *J. Climate*, **13**, 1574–1592.

Figure

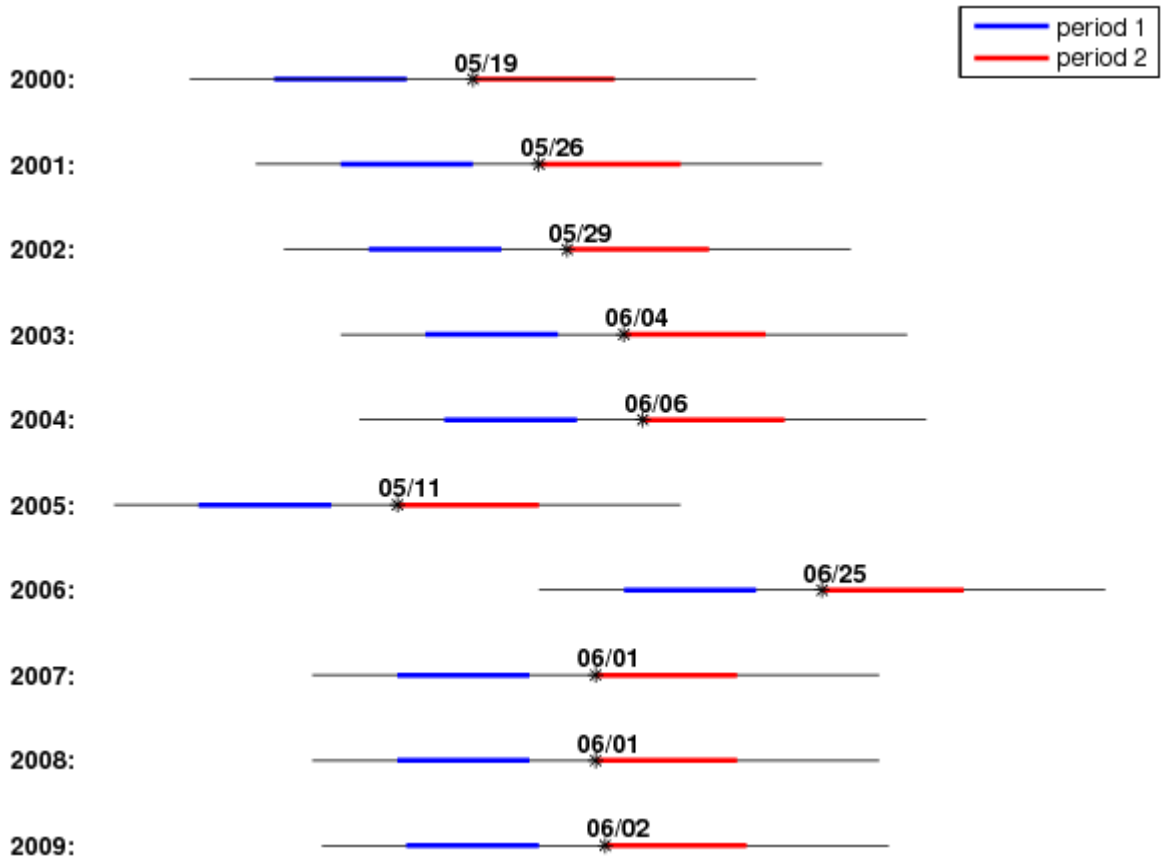

Figure 1 : reference dates Tref for each particular year, from 2000 to 2009 (black star), with ≪ period 1 ≫ (from [Tref - 3 weeks] until [Tref – 1 week], blue line) and ≪ period 2 ≫ (from Tref until [Tref + 2 weeks], red line).

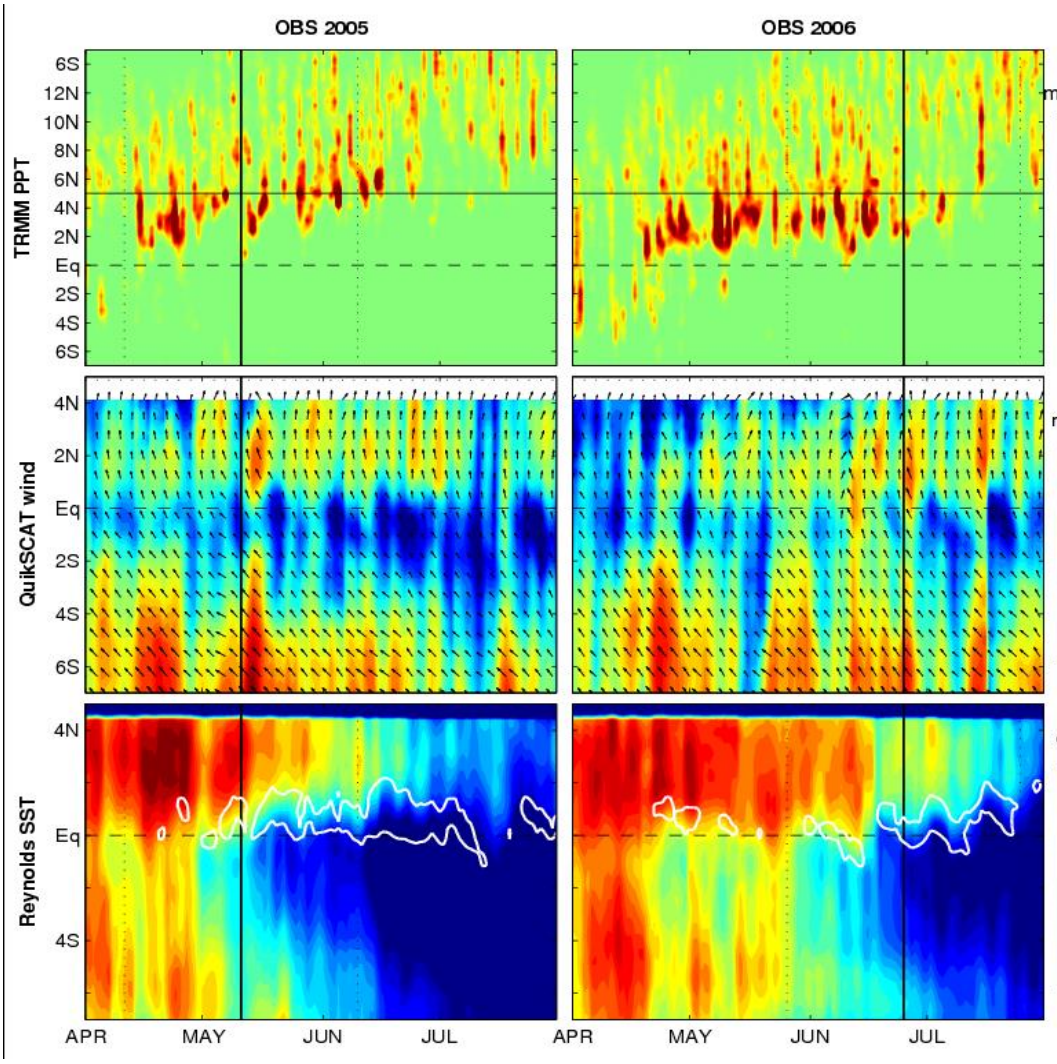

Figure 2: diagram time / latitude of TRMM precipitation (top), QuikSCAT surface wind (middle, speed in shadings) and Reynolds SST (bottom), 10° W–0, in May–June–July–August 2005 (left) and 2006 (right). White contour in the lower row indicates a SST meridional gradient of 0.6 K per latitude degree. Vertical black line points Tref, and black dotted lines frame a period of 2 months around Tref.

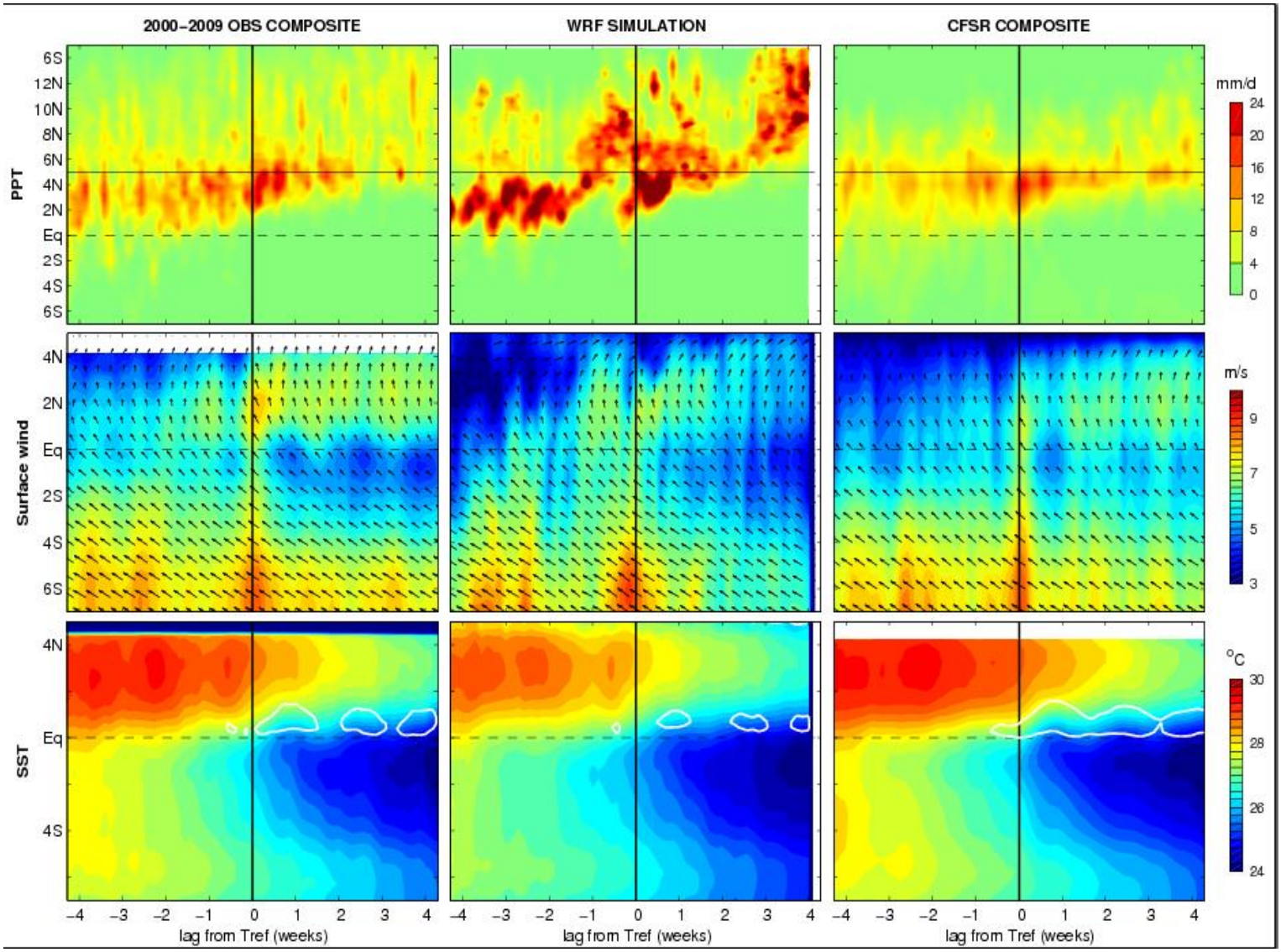

Figure 3: time / latitude diagrams of ~2-month composites around the date of reference Tref, 10° W-0: in the observations (left column), in the WRF simulation (middle), and in the CFSR ranalysis (right) ; of PPT (top row), surface wind (middle) and SST (bottom, SKT for WRF). Black vertical lines indicate Tref. White contours in lower frames indicate level 0.6 K per latitude-degree for the SST (OBS and CFSR) or SKT (WRF output) meridional gradient.

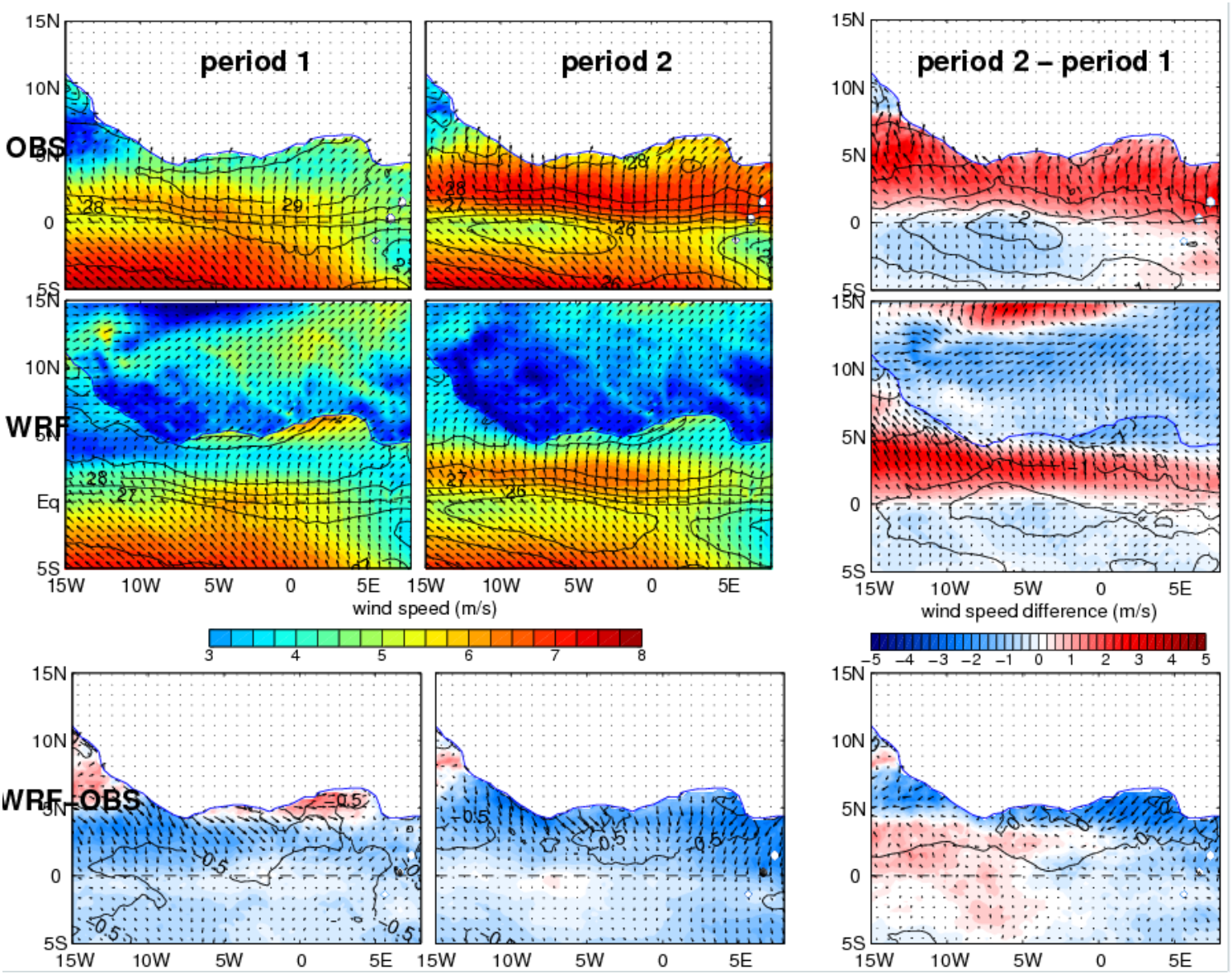

Figure 4: Top row: observed QuikSCAT surface wind velocity (speed in shadings, m/s) and Reynolds SST (black contours), averaged in Period 1 (i.e. from Tref−3 weeks to Tref−1 week, left), Period 2 (average from Tref to Tref+2 weeks, middle column), and their difference (right). Middle row: similar than top row, but for the WRF simulation with SKT instead of SST (SKT not plotted over the continent for clarity). Bottom row: differences between top and middle rows (WRF−OBS).

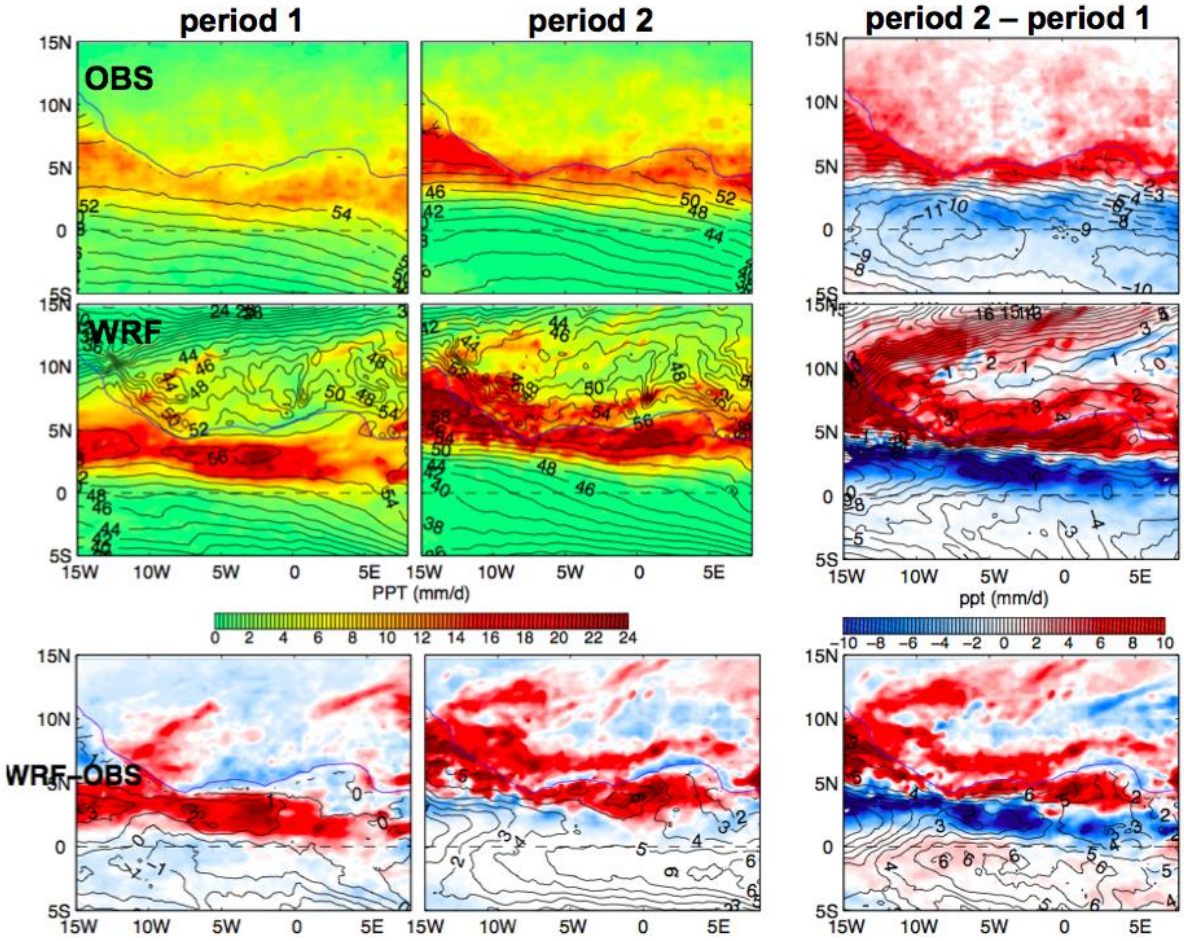

Figure 5: similar than Fig. 4, but for precipitation (shadings, in mm/day, observations from the TRMM B42 product) and precipitable water vapor (black contours, intervals of 2 kg/m2).

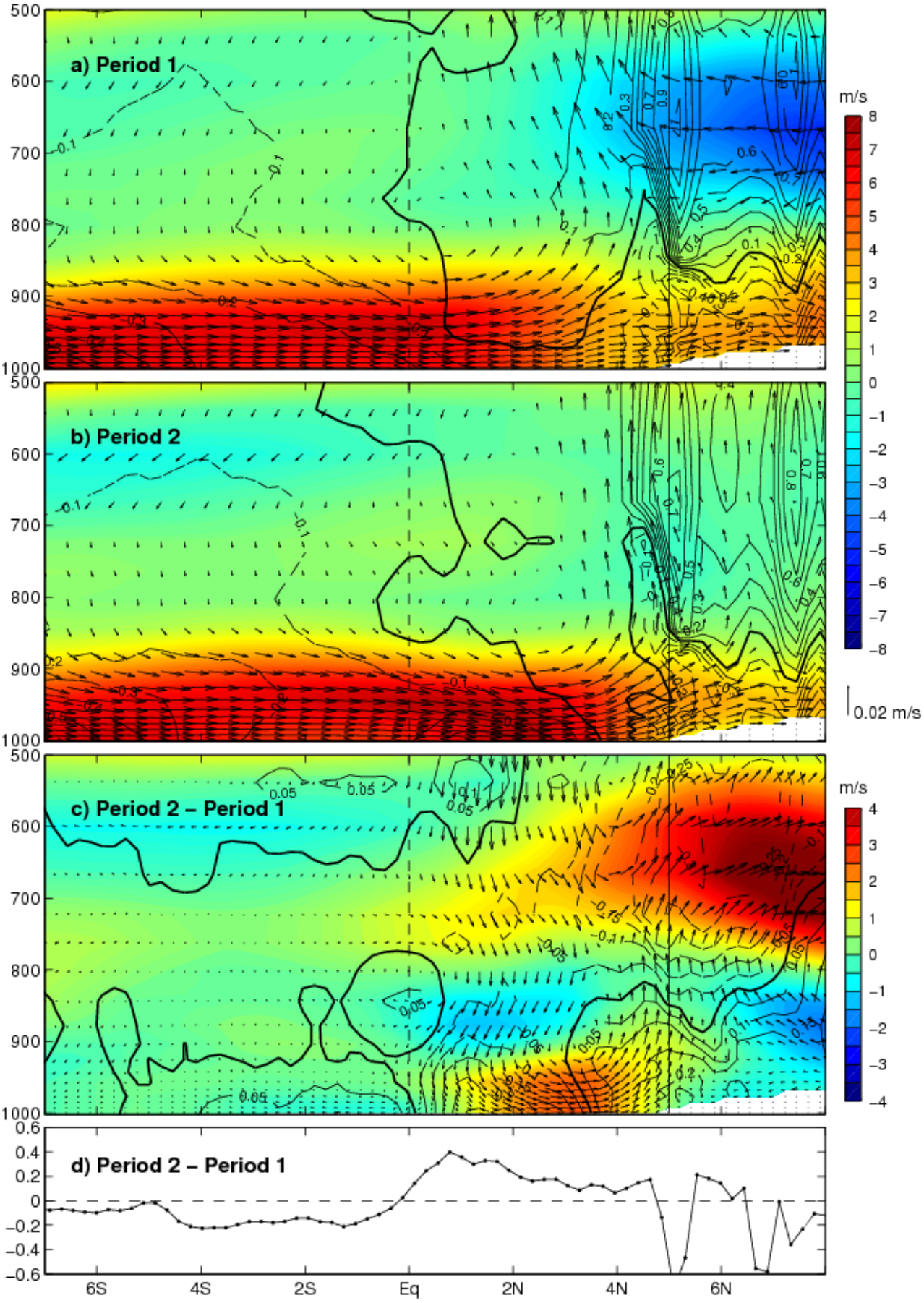

Figure 6: 10° W-0, WRF simulation composites ≪ Period 1 ≫ (a), ≪ Period 2 ≫ (b) and ≪Period 2 ≫ minus ≪ Period 1 ≫ (c) of meridional wind (shadings) and meridional gradient of geopotential height (black contours, intervals of 0.1 m per lat. degree for a and b, or 0.05 m per lat. degree for c, level 0 in heavy black). (d): ≪Period 2 ≫ minus ≪ Period 1 ≫ of the meridional gradient of SKT (K per lat. deg.). Vertical dashed line stands fo the equator latitude, plain for the Guinean

coast mean latitude (5° N).

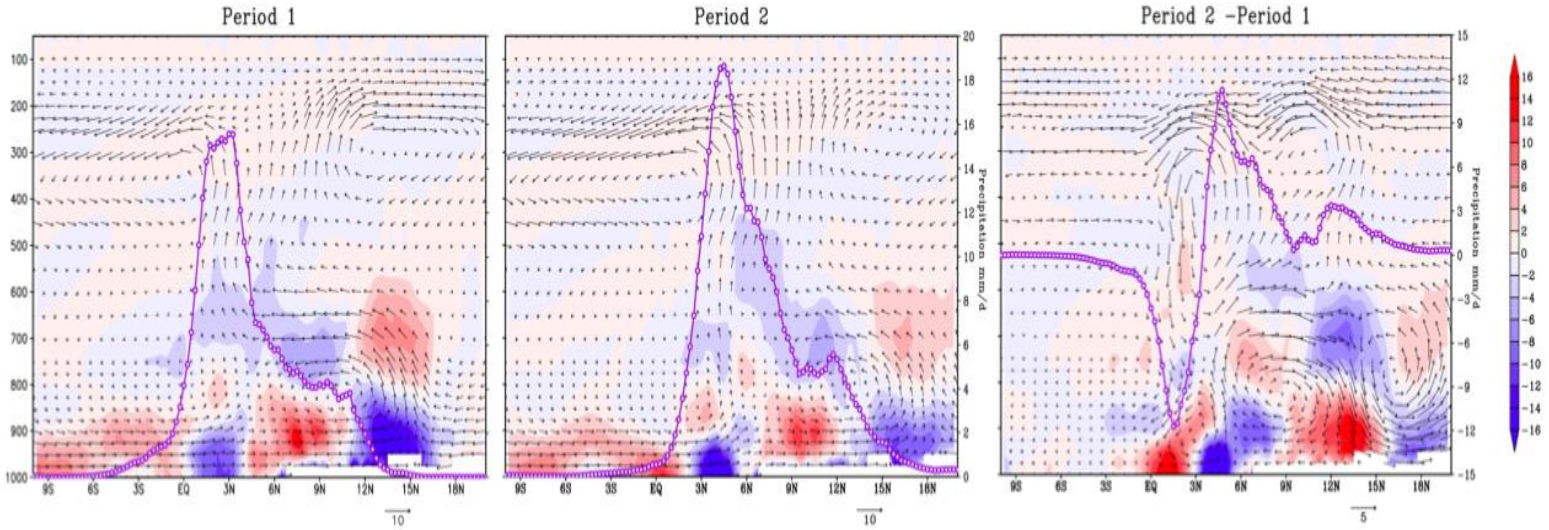

Figure 7: 10° W-0 WRF simulation averages in period 1 (left), period 2 (middle) and their difference (right), of the meridional humidity divergence (shadings, kg/mˆ3/s), the meridional circulation (arrows) and the precipitation (magenta profile, mm/day).

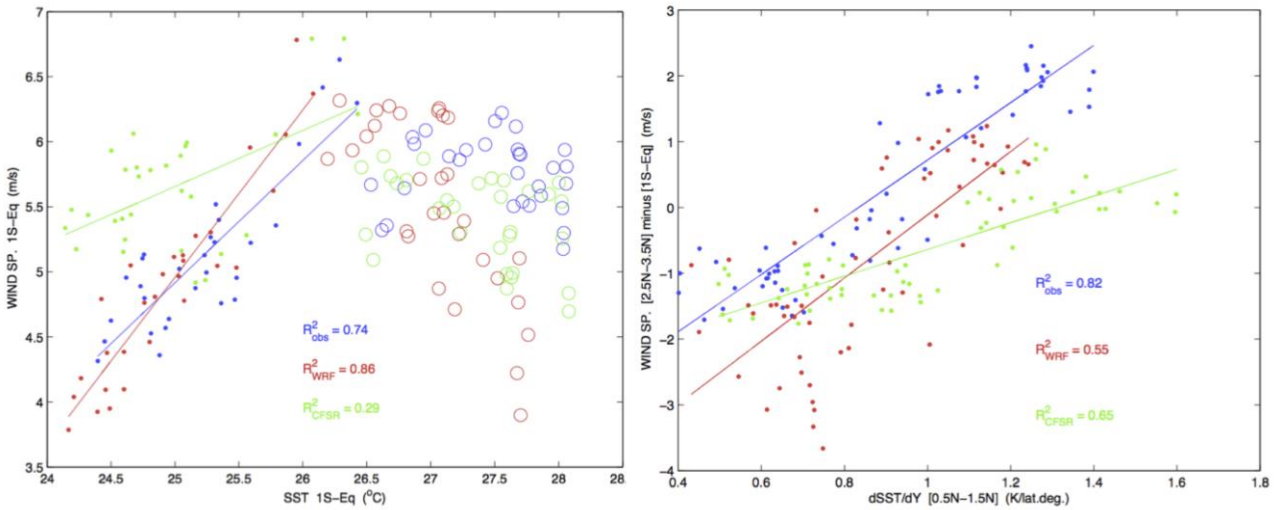

Figure 8: Left: composites of daily surface wind speed versus daily SST, 2000–2009, 10° W–0 / 1° S–Eq, 30 days before (circles) and 30 days after (dots) Tref, in the observations (blue) and CFSR reanalyses (green), or in the corresponding WRF simulation (red). Lines : linear ≪ least square fit ≫ regressions. Right: similar, but for the surface wind speed difference ([2.5° N–3.5° N] minus [1° S–Eq]) versus dSST/dY ([Eq–1° N]). The coefficient of determination is indicated for each regression.

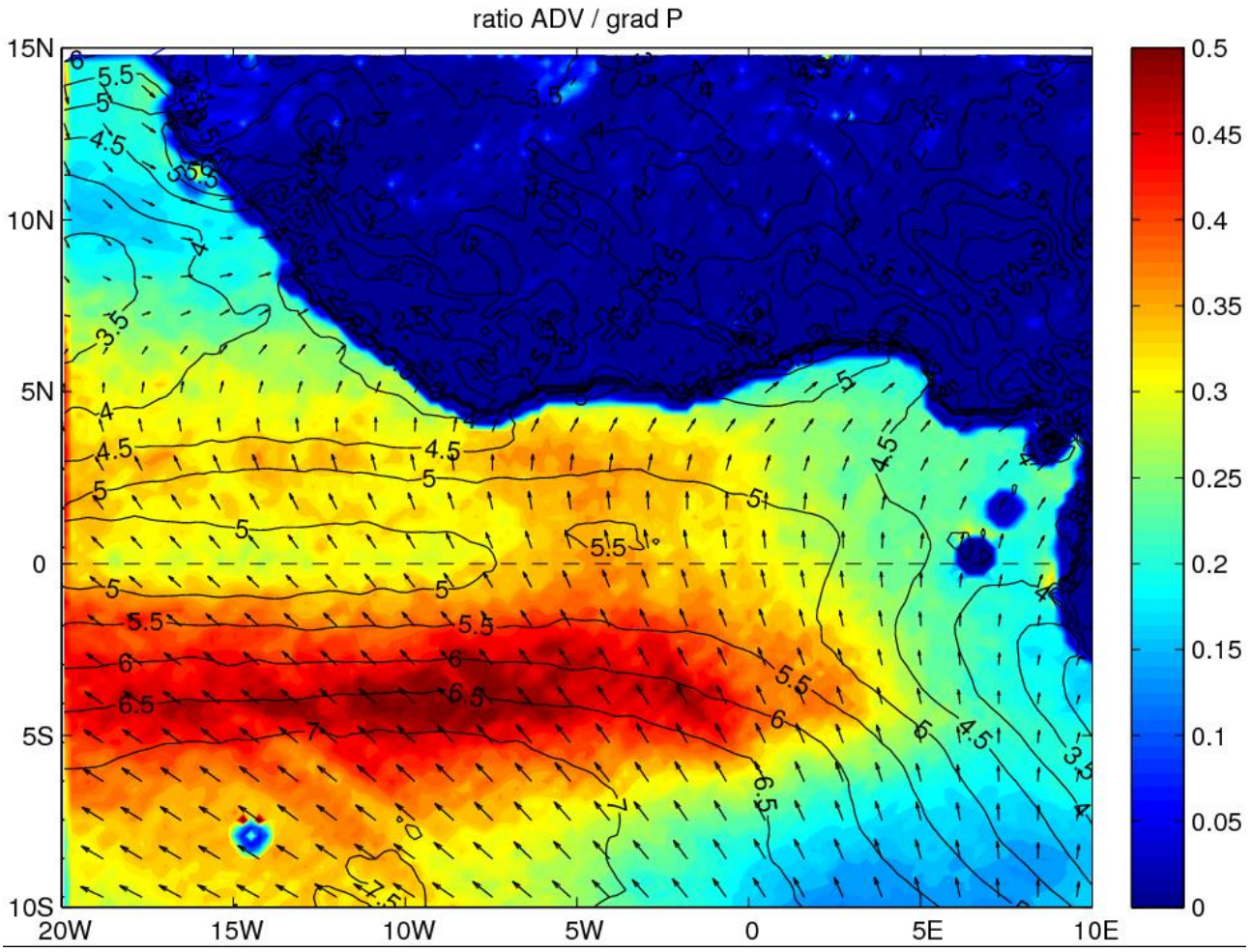

Figure 9: In the WRF simulation, fraction of the advection (inertial) term $\|\vec{U}.\nabla\vec{U}\|$, versus the pressure gradient term $\frac{1}{\rho}\|\nabla SLP\|$ where $\rho = 1.12\,kg/m^3$ (shading). Mean $\vec{U}$ (arrows) and wind speed $\|\vec{U}\|$ (black contours, intervals of 0.5 m/s). All terms were first computed at the simulation output frequency (i.e. 8 values per day during the 2-month simulation around Tref), and then averaged over the whole period.

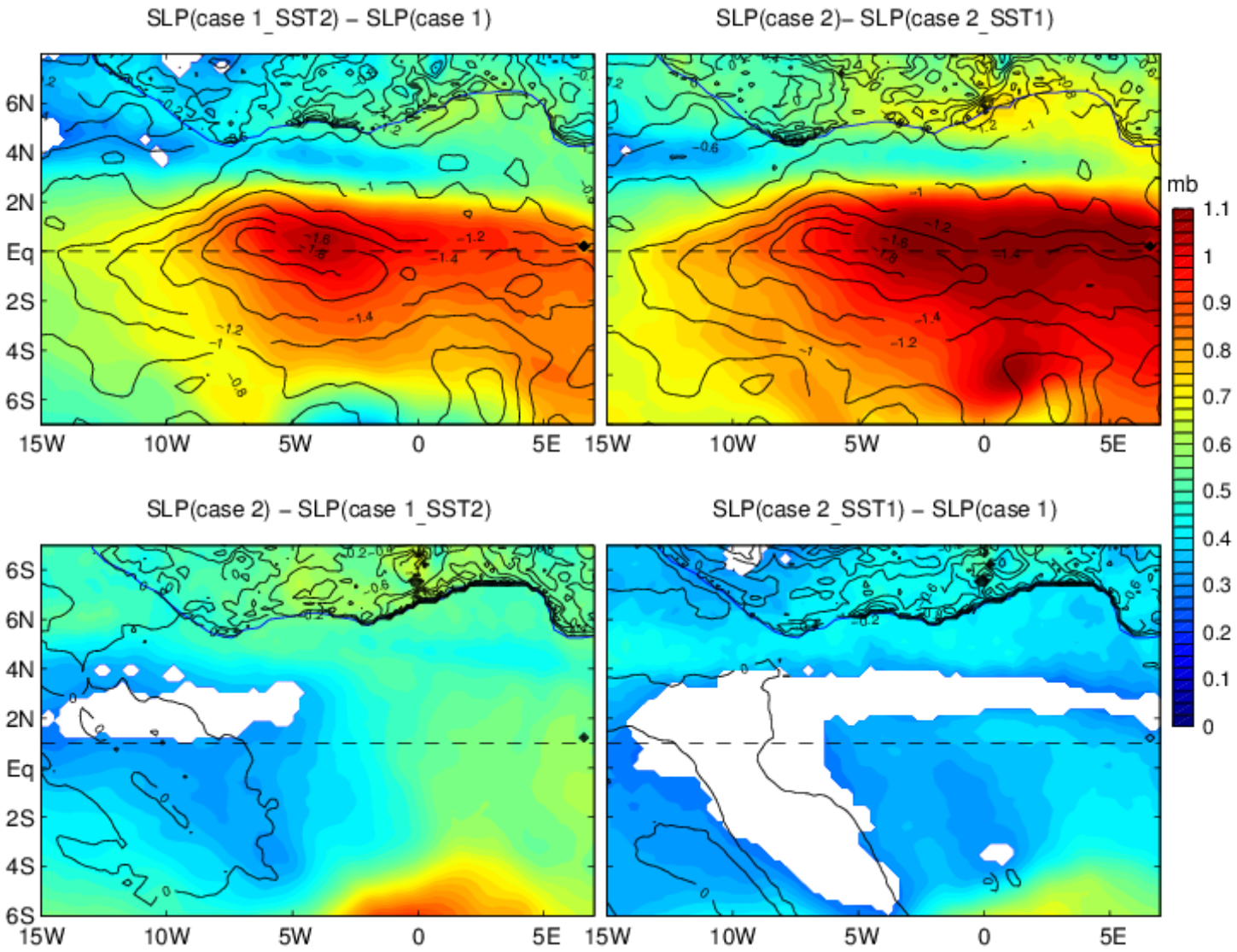

Figure 10: WRF simulation surface pressure (colours) and SST (black contours, intervals of 0.2 K) differences between:

* testing the influence of the SST :

case 1 with SST2 - case 1 (top left), and case 2 - case 2 with SST1 (top right);

* testing the influence of the external forcing :

case 2 - case 1 with SST2 (bottom left), case 1 with SST2 - case 2 (bottom right).

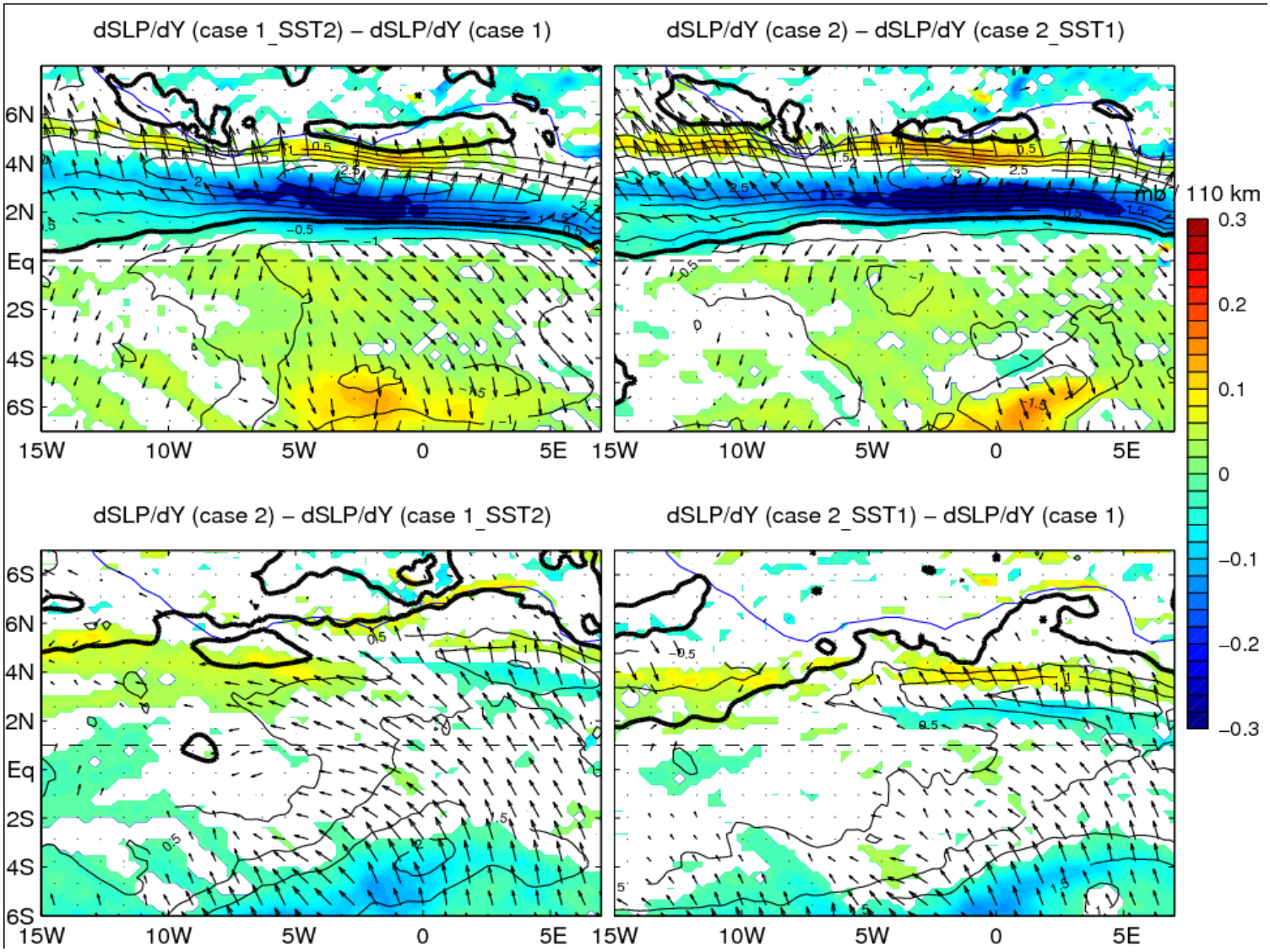

Figure 11: same as Fig. 5 for the absolute value of pressure gradient (shadings) and wind speed (black contours, intervals of 0.5 m/s, heavy line marks null wind speed difference).

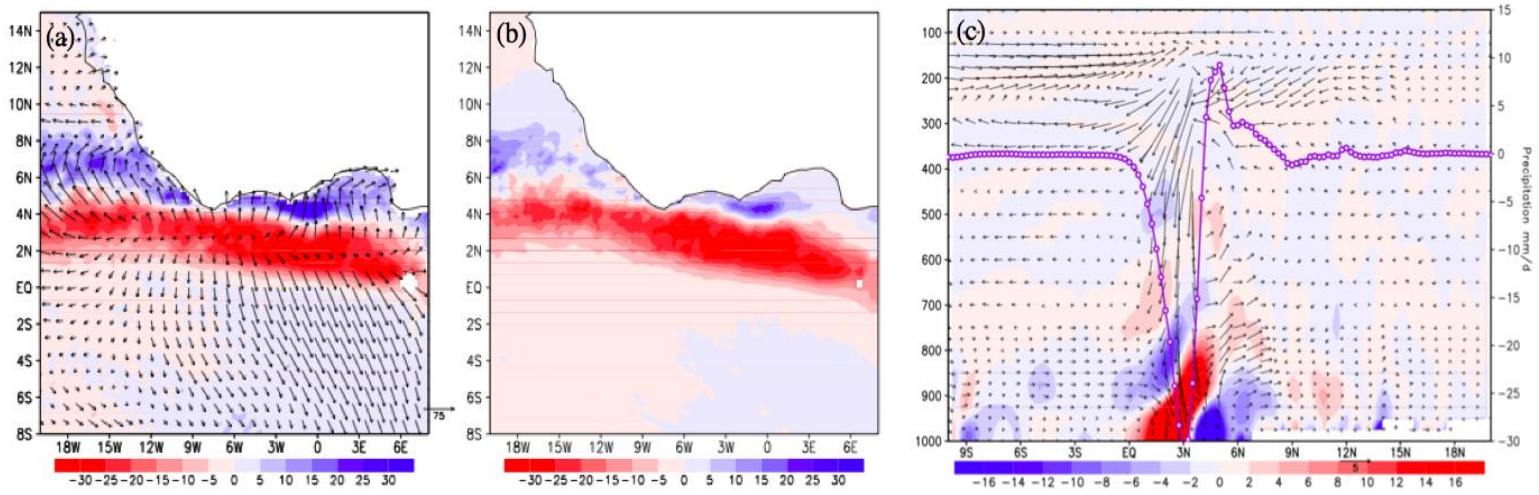

Figure 12: In WRF simulation : testing the influence of the SST with ≪ Case 2 ≫ minus ≪ Case 2 with SST1 ≫ for : a) vertically integrated Moisture flux convergence (divergence) in blue (red), in mm/day, with integrated moisture flux ($kg/m^2/s$), (b) precipitation (mm/day), (c) zonal average (10° W-0W) of vertical cross section of horizontal moisture flux divergence (shading, EMBED opendocument.MathDocument.1 $10^8 s^{-1}$), meridional (m/s) - vertical (×100 Pa/s)